Arabian Journal of Chemistry (2023) **16**, 104950

King Saud University

Arabian Journal of Chemistry

www.ksu.edu.sa
www.sciencedirect.com

ORIGINAL ARTICLE

Adsorption of PO_4^{3-}, Cd(II), Pb(II), Cu(II), As(III), and As(V) using a carbonised Mn-based metal–organic framework

Yating Chen [a,b,1], **Zhao Chen** [b,c,1], **Lingyu Yuan** [b], **Yu Xiao** [a], **Shu-Hua Zhang** [a,b,*], **Ning Li** [a,*]

[a] *Guangdong Provincial Key Laboratory of Petrochemical Pollution Process and Control, Key Laboratory of Petrochemical Pollution Control of Guangdong Higher Education Institutes (College of Chemistry), Guangdong University of Petrochemical Technology, Maoming, Guangdong 525000, PR China*
[b] *Guangxi Key Laboratory of Electrochemical and Magnetochemical Functional Materials (College of Chemistry and Bioengineering), Guilin University of Technology, Guilin 541004, PR China*
[c] *CEPREI Innovation (Chongqing) Technology Co., LTD, Shapingba District, Chongqing 401332, PR China*

Received 17 December 2022; accepted 24 April 2023
Available online 28 April 2023

KEYWORDS

Mn-MOF-500;
Adsorption;
PO_4^{3-};
Heavy metal ions

Abstract Metal–organic frameworks (MOFs) are adsorbents suitable for water treatment. However, they are often water soluble and poorly processible, limiting their industrial applications. This study aims to develop a carbonized MOFs with high adsorption performance based on MOFs. Here, we report the production of **Mn-MOF** $[Mn(DMF)_2(H_2DHTPA)]_n$ (where DMF is *N*,*N*-dimethylformamide and H_4DHTPA is 2,5-dihydroxyterephthalic acid) *via* a solvothermal method. This MOF shows good adsorption performance for various ions but dissolves easily in water. However, **Mn-MOF-500** which was obtained by carbonising **Mn-MOF** at 500 °C shows high water stability. Thus, the adsorption properties of **Mn-MOF-500** were investigated, revealing adsorption capacities for PO_4^{3-}, Cd(II), Pb(II), Cu(II), As(III), and As(V) of 126.66, 88.46, 356.21, 146.92, 51.28, and 166.10 mg/g, respectively. Based on the adsorption isotherms and the adsorption kinetics, the adsorption of PO_4^{3-}, Cd(II), and As(III) occurs *via* monolayer chemisorption, whereas that of Pb(II), Cu(II), and As(V) occurs *via* monolayer chemisorption and physisorption in pores. X-ray diffractometry and X-ray photoelectron spectroscopy analysis showed that P, Cd(II), Pb(II), Cu (II), As(III), and As(V) were adsorbed on **Mn-MOF-500** as PO_4^{3-}, $Cd(OH)_2$, PbO and $Pb(OH)_2$, $Cu(OH)_2$, $Mn_3(AsO_3)_2$, and $MnHAsO_4$, respectively.

---

[*] Corresponding authors.
E-mail addresses: Zhangshuhua@gdupt.edu.cn (S.-H. Zhang), liningmmc@gdupt.edu.cn (N. Li).
[1] Yating Chen and Zhao Chen contributed equally to this work.

https://doi.org/10.1016/j.arabjc.2023.104950
1878-5352

1. Introduction

Increasing industrial development has resulted in environmental problems, such as the production of acidic wastewater from mining, and this is a global problem (Krupskaya and Zvereva, 2014). The primary methods for removing contaminants from acid mine wastewater are physical, chemical, biological, and microbial methods, which include precipitation, adsorption, ion exchange, electrochemical treatment technology, and biochemical methods (Ríos, et al., 2008; Yilmaz, et al., 2005; Vymazal, 2007; Türker, et al., 2014; Fosso-Kankeu, et al., 2011; Vignesh et al., 2014). Adsorption can occur *via* chemical and physical processes, and this method has been favoured by researchers for wastewater treatment because of its simplicity, efficiency, and low cost (Yilmaz, et al., 2005; Zhang, et al. 2021c; Zhang, et al. 2023). As a result, the development of adsorbents is a hot topic. Metal–organic framework materials (MOFs) are relatively new adsorbents showing high chemical and physical stability, high specific surface areas, a large number of active sites, and adjustable pore sizes, thus having advantages over activated carbon, zeolite, and minerals such as titanium dioxide and other traditional materials (Li, et al., 1999; Chen, et al., 2019; An, et al., 2018; Bhadra, et al., 2017; Li, et al., 2018; Oveisi, et al., 2018; Song, and Jhung, 2017; Zhang, et al., 2022; Wang, et al., 2021b; Zhang, et al., 2021c; Yu, et al., 2020; Wu, et al., 2019b; Dutta, et al., 2021; Liu, et al., 2020a; Zhang, et al. 2023). For example, Liu, et al., reported Zr-modified chitosan beads having a high adsorption capacity for phosphate ions, reaching 60.60 mg/g (Liu and Zhang, 2015); Veenhuyzen, et al., reported a waste activated sewage sludge (WAS) having an adsorption capacity for Pb (II) of 307 mg/g (Veenhuyzen, et al., 2015); and Zhou et al., reported a ZSM-5 zeolite supporting sulfide nanoscale zero-valent iron (S-nZVI@ZSM-5) having an adsorption capacity for As (V) of 161.66 mg/g (Zhou, et al., 2021).

Many MOF-based adsorbents have been reported in recent years, however, most MOF materials are only used for adsorption treatment of one pollution factor (Zhang, et al., 2021c; Yu, et al., 2019) while the adsorbents studies of the MOFs have not been comprehensive. We have found that MOFs have high adsorption capacities for various pollutants (Wang, et al., 2021b; Zhang, et al. 2022a). Then, since some of the materials were synthesized with water as the solution, there was a phenomenon of decomposition in the aqueous solution, which was not conducive to being used as a water adsorption material.

In recently years, Mn-base MOFs have gotten a lot of attentions (Mbonu and Abiola, 2021; Chao, et al., 2020; Xu, et al., 2013), because the Mn-MOFs can be used as electrocatalysis, adsorbent, magnetic materials, et al.

In this study, to overcome this disadvantage, a Mn-based MOF sorbent was carbonized at a high temperature to yield a carbon-based MOF composite material, and its adsorption performance was studied. Specifically, our MOF, denoted **Mn-MOF** ($[Mn(DMF)_2(H_2DHTPA)]_n$), where DMF is *N*,*N*-dimethylformamide and H_4DHTPA is 2,5-dihydroxyterephthalic acid, was synthesized by the solvothermal method. Carbonising **Mn-MOF** at 500℃ yielded **Mn-MOF-500**, which showed high water stability and good adsorption performance. The **Mn-MOF-500** was used for the adsorption of phosphate and heavy metal ions (Cd(II), Pb(II), Cu(II), As(III), and As(V)) from simulated acid mine wastewater. The adsorption properties were analysed by adsorption experiments, and the adsorption mechanism was characterized by powder X-ray diffractometry (PXRD), Fourier transform infrared (FT-IR) spectrometry, X-ray photoelectron spectroscopy (XPS), and scanning electron microscopy (SEM).

2. Experiments and methods

2.1. Synthesis of Mn-MOF and Mn-MOF-*n* (*n* = 300, 400, 500, 600, 700, and 800 °C)

A mixture of H_4DHTPA (5 mmol, 0.990 g), 1,3-di(4-pyridyl) propane (5 mmol, 0.990 g), $MnCl_2{\cdot}4H_2O$ (10 mmol, 1.979 g), and DMF (100 mL) was stirred for 30 min, and the pH was adjusted to 6 by addition of triethylamine. Then, the mixture was sealed in a 200-mL Teflon-lined stainless-steel vessel and heated at 150 °C for 48 h in an oven and slowly cooled to room temperature. Colorless block-shaped crystals were collected, washed with DMF, and dried in air. Phase pure crystals of **Mn-MOF** were obtained by manual separation (yield: 0.814 g, *ca.* 82.20 % based on H_4DHTPA). *Anal. Calcd.* For **Mn-MOF**: $C_{14}H_{18}MnN_2O_8$ (M_r = 396.94), *calcd.*: C, 42.32; H, 4.53; N, 7.06%. Found: C, 42.26; H, 4.61; N, 7.15%. FT-IR data for **Mn-MOF** (Fig. S1, KBr, cm^{-1}): 3384.2(vs), 2935.9(s), 1646.1(s), 1590.7(s), 1446.0(s), 1236.9(s), 1105.5(s), 781.5(s), 1491.2(m), 1387.5(m), 915.9(m), 860.7(m), 614.6 (m).

Mn-MOF-*n* (*n* = 300, 400, 500, 600, 700, and 800 °C). **Mn-MOF-*n*** were obtained by carbonising the **Mn-MOF** (1 g) in a tube furnace under oxygen conditions at the corresponding temperatures (*n* = 300, 400, 500, 600, 700, and 800 °C) for 240 min and allowing the samples to cool to room temperature.

2.2. Adsorption experiments and characterization

Relevant adsorption experiments, characterisation methods, and equations are shown in the Supporting Material, Section 1.2.

2.3. Single-crystal X-ray crystallography

Single-crystal X-ray diffraction data of **Mn-MOF** was collected on an Agilent G8910A CCD diffractometer with graphite monochromated Mo-K_α radiation (λ = 0.71073 Å) at 20 ± 1 °C in ω-θ scan mode. Raw frame data were integrated using SAINT, and the structure was solved using direct methods with SHELXT (Sheldrick, 2015) and refined by full-matrix least-squares on F^2 using SHELXL-2018 within the OLEX-2 GUI (Dolomanov, et al., 2009). An empirical absorption correction was applied with spherical harmonics, as implemented in the SCALE3 ABSPACK scaling algorithm. All non-hydrogen atoms were refined anisotropically, and all hydrogen atoms were positioned geometrically and refined using the riding model. Calculations and visualisation were achieved using SHELXTL (Sheldrick, 2015). The crystallographic details are provided in Table S1. Selected bond lengths and angles for **Mn-MOF** are listed in Table S2.

3. Results and discussion

3.1. *Crystal structure of $[Mn(DMF)_2(H_2DHTPA)]_n$ (Mn-MOF)*

The reaction of H_2DHTPA, 1,3-di(4-pyridyl)propane, $MnCl_2\cdot 4H_2O$, and DMF (100 mL) at 150 °C for 48 h, the **Mn-MOF** was synthesized (Scheme 1). The 1,3-di(4-pyridyl)propane ligand does not participate in the coordination.

The single-crystal X-ray diffraction analysis revealed that **Mn-MOF** crystallised in the monoclinic crystal system and the *I*2/*a* space group (Fig. 1, Table S1), and the asymmetric unit contained one crystallographically independent Mn(II) ion, one H_2DHTPA ligand, and two DMF ligands, as shown in Fig. 1. Mn1 is six-coordinated by four oxygen (O) atoms from the carboxyl group of the four different H_2DHTPA ligands (Mn1 – O3, 2.146(2) Å; Mn1 – O2B, 2.169(2) Å; symmetry code: (B) $\times$ -0.5, y + 0.5, z + 0.5.) and two O atoms from the two different DMF molecules (Mn1 – O1, 2.187(2) Å). Thus, Mn1 forms a slightly distorted octahedral geometry, whereas the *cis*-O-Mn-O bond angles are 180° (O1-Mn1-O1A; O3-Mn1-O3A; O2B-Mn1-O2C, 180°, symmetry codes: (A) 0.5 – x, y + 1, – z; (C) 2 – x, 1.5 + y, 0.5 – z.). The Mn-MOF forms a dinuclear unit through double carboxyl group bridges, which further form a 1D chain through carboxyl group bridge expansion (Fig. S2). The 1D chain constructed a 3D network through $\eta^1:\eta^1:\eta^1:\eta^1$-$\mu_4$-$H_2$DHTPA bridge ligands (Fig. S3). Interestingly, there are strong intramolecular O-H···O hydrogen bonds (O4···O3, 2.586(3) Å), and the porosity of **Mn-MOF**, as calculated by Platon, is 53.6% (based on the omission of the DMF molecules), and a one-dimensional rhombus-shaped channel can be seen in the direction of the *a*-axis; the channel size is 15.288(1) × 11.986(2) Å ^{2} (Fig. 2). Herein, the distance of 15.288(1) Å is Mn1···Mn1^i distance (symmetry code: (i) $\times$ – 1, y – 1, z.) while the distance of 11.986(2) Å is O2···O2^{ii} distance (symmetry code: (ii) −0.5 – x, y, 1 – z.). In the one-dimensional rhombus-shaped channel, manganese atoms are not saturated in coordination and there are uncoordinated hydroxyl oxygen atoms.

3.2. *Selection of optimum carbonization temperature*

As shown in Table 1, **Mn-MOF** showed good adsorption for PO_4^{3-}, Cd(II), Pb(II), Cu(II), As(III), and As(V) ions. For **Mn-MOF-*n***, the adsorption behaviors for the six ions were different. The adsorption capacities of **Mn-MOF-*n*** for the ions increased with the increase of carbonisation temperature, but, after carbonisation 500 °C, the adsorption capacity decreased. Thus, the optimal carbonisation temperature was 500 °C, and **Mn-MOF-500** was used for subsequent studies.

3.3. *Adsorption performance analysis of MN-MOF-500*

3.3.1. *Single-factor experiment of Mn-MOF-500*

The pH and adsorbent dosage are important factors in adsorption experiments. Thus, the influence of these factors on the sorption of PO_4^{3-}, Cd(II), Pb(II), Cu(II), As(III), and As(V) was investigated, as detailed in the Supporting Material, Section 1.3.1. The optimum pH for the adsorption of the six ions by **Mn-MOF-500** was pH 5, and the optimum dosage for PO_4^{3-}, Pb(II), Cu(II), and As(V) ions was 0.02 g, whereas that for Cd (II) and As(III) was 0.05 g.

3.3.2. *Adsorption isotherm fitting*

The adsorption mechanism and adsorption capacity were investigated using adsorption experiments. Fitting of the data to the Langmuir and Freundlich adsorption isotherms for PO_4^{3-}, Cd(II), Pb(II), Cu(II), As(III), and As(V) at 288, 298, and 308 K was carried out, and the results are detailed in Table 2 and Fig. 3.

The coefficients of determination (R^2) of the Langmuir model for PO_4^{3-} adsorption were 0.99, 0.99, and 0.99 at 288, 298, and 308 K, respectively, higher than those of the Freundlich model at the same temperatures (0.91, 0.93, and 0.94, respectively). The results show that the adsorption of PO_4^{3-} is monolayer adsorption, and the adsorption capacity is the same over the whole surface of the adsorbent. For the Langmuir model, the maximum adsorption capacities ($q_{\max}$) of **Mn-MOF-500** for PO_4^{3-} at 288, 298, and 308 K were

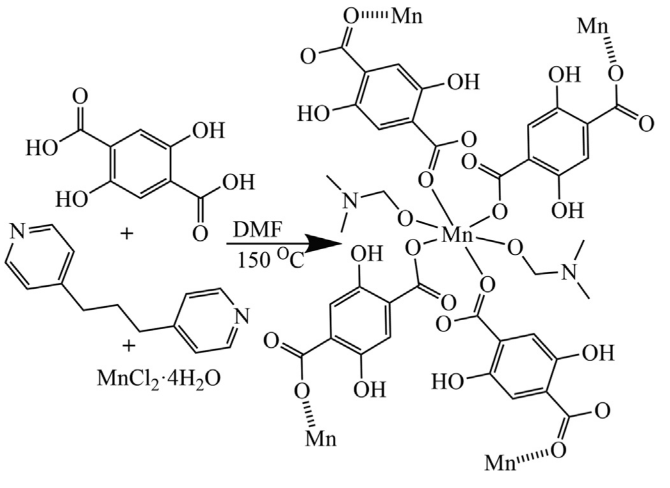

Scheme 1 Synthetic routes for Mn-MOF.

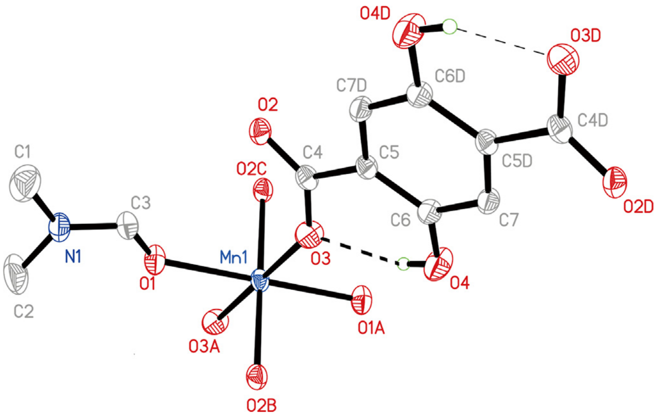

Fig. 1 Molecule structure of **Mn-MOF**.

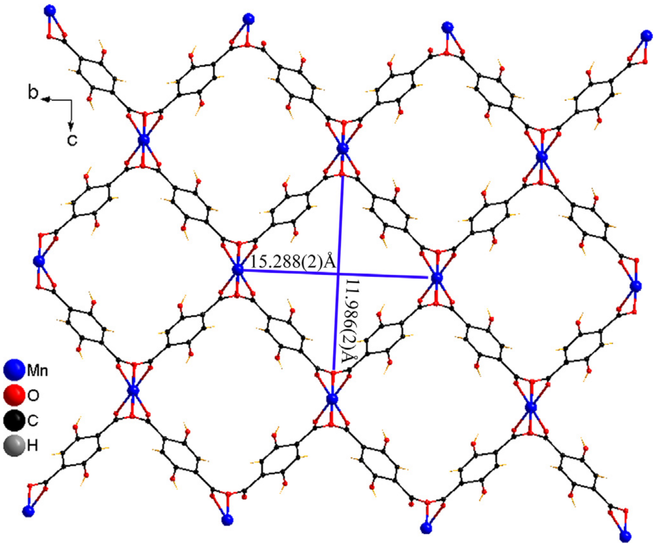

Fig. 2 3D network of **Mn-MOF,** omitted the DMF molecules.

Table 1 The removal rate of six ions by **Mn-MOF** and **Mn-MOF-n** (%).

Ions	**Mn-MOF**	300 °C Mn-MOF	400 °C Mn-MOF	500 °C Mn-MOF	600 °C Mn-MOF	700 °C Mn-MOF	800 °C Mn-MOF
PO_4^{3-}	93.08%	58.74%	66.82%	73.42%	69.54%	60.96%	53.08%
Cd(Ⅱ)	79.46%	39.72%	85.52%	93.34%	77.76%	38.32%	33.84%
Pb(Ⅱ)	98.04%	96.44%	98.21%	99.45%	95.22%	53.52%	80.81%
Cu(Ⅱ)	95.36%	48.94%	75.44%	96.91%	33.80%	13.62%	40.08%
As(III)	83.08%	9.48%	61.54%	79.16%	66.82%	39.16%	26.84%
As(V)	92.88%	39.48%	73.52%	96.88%	78.62%	57.28%	43.54%

79.38, 98.26, and 126.88 mg/L, respectively. The greatest value of $q_{\max}$ (126.88 mg/L) was obtained for PO_4^{3-} (Liu and Zhang, 2015; Biswas et al., 2007; Xu et al., 2009; Köse and Kıvanç, 2011; Anirudhan et al., 2006).

For Cd(II), Pb(II), and Cu(II) ions, the Langmuir model fitted the data better than the Freundlich model, as shown by the R^2 values (Table 2), indicating monolayer, homogenous adsorption on the surface of the material. The $q_{\max}$ values for Cd(II) are 72.21, 86.57, and 88.46 mg/g, respectively, The $q_{\max}$ values for Pb(II) are 257.83, 318.07, and 356.21 mg/g, and The $q_{\max}$ values for Cu(II) are 122.00, 129.84, and 146.92 mg/g at 288, 298, and 308 K, respectively. Further, the $q_{\max}$ values are 88.46, 356.21, and 146.92 mg/g for Cd (II), Pb(II), and Cu(II) ions, respectively, which are the largest reported values for the sorption of Cd(II) (Liu, et al., 2021; Xie, et al., 2021; Zhang, et al., 2021d; Ahmed, et al., 2020; Xu, et al., 2021), Pb(II) (Veenhuyzen, et al., 2021; Wang, et al., 2019a; Shi, et al., 2021; Wu, et al., 2019a; Wang,

Table 2 Isotherm parameters of **Mn-MOF-500** adsorption PO_4^{3-}, Cd(II), Pb(II), Cu(II), As(III), and As(V).

Ions	T(K)	q_{maxEX}* / (mg/g)	Langmuir			Freundlich		
			q_{max} / (mg/g)	b (L/mg)	R^2	K_F	n	R^2
PO_4^{3-}	288	75.69	79.38	0.06	0.99	12.86	2.90	0.91
	298	93.83	98.26	0.05	0.99	14.84	2.77	0.93
	308	121.30	126.88	0.05	0.99	17.82	2.63	0.94
Cd(II)	288	71.97	74.21	0.08	0.99	12.28	2.63	0.95
	298	82.71	86.57	0.09	0.99	14.36	2.55	0.96
	308	86.31	88.46	0.10	0.99	16.69	2.65	0.96
Pb(II)	288	262.43	257.83	0.54	0.99	95.57	5.52	0.91
	298	321.3	318.07	1.25	0.98	134.60	6.01	0.87
	308	357.6	356.21	2.53	0.97	165.61	6.62	0.84
Cu(II)	288	117.68	122.00	1.29	0.95	40.13	4.93	0.81
	298	125.18	129.84	1.83	0.93	43.66	5.02	0.81
	308	145.13	146.92	2.65	0.99	53.86	5.21	0.84
As(III)	288	37.47	38.17	0.06	0.98	6.84	3.04	0.95
	298	43.11	43.55	0.24	0.99	11.06	3.68	0.93
	308	50.79	51.28	0.24	0.98	12.43	3.52	0.95
As(V)	288	122.70	126.90	0.05	0.99	19.25	2.94	0.90
	298	143.93	150.99	0.07	0.99	24.95	3.03	0.88
	308	160.58	166.10	0.09	0.99	31.14	3.20	0.88

* q_{maxEX} means experimental value q_{max}.

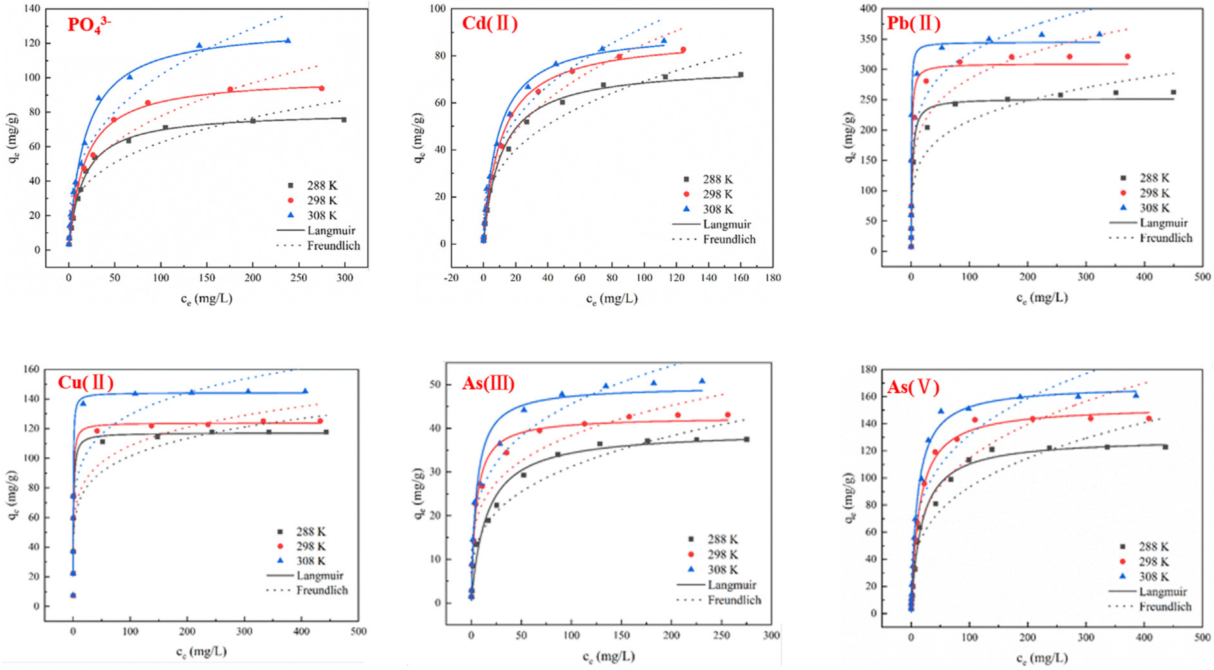

Fig. 3 Nonlinear fitting to the Langmuir and Freundlich models of the adsorption of PO_4^{3-}, Cd(II), Pb(II), Cu(II), As(III), and As(V) over Mn-MOF-500.

et al., 2021c), Cu(II) ions (Liu, et al., 2020b; He, et al., 2020; Zhang, et al., 2021a; Zhang, et al., 2021b; Jin, et al., 2021), respectively.

For the adsorption of As(III), and As(V) ions, the data fitted the Langmuir model better than the Freundlich model based on the R^2 values (Table 2), indicating mainly monolayer adsorption. The q_{max} values of Mn-MOF-500 for As(III) were 38.17, 43.55, and 51.28 mg/g, respectively, and those for As(V) were 126.90, 150.99, and 166.10 mg/g at 288, 298, and 308 K, respectively. The q_{max} values were 51.28, 166.10 mg/g for As (III), As(V) ions, respectively, which are the largest reported values for the sorption of As(III) (Wang, et al., 2021a; Pervez, et al., 2021; Lin, et al., 2019; Mudzielwana, et al., 2019; Dong, et al., 2020), As(V) ions (Zhou, et al., 2021;

Pervez, et al., 2021; Mahato, et al., 2021; Wang, et al., 2019b; Salih, et al., 2019), respectively.

Fitting to the Freundlich model yielded $n \geq 1$ for PO_4^{3-}, Cd(II), Pb(II), Cu(II), As(III), and As(V) ions at the three temperatures, indicating facile adsorption and $q_{\max}$ of **Mn-MOF-500** on PO_4^{3-}, Cd(II), Pb(II), Cu(II), As(III), and As(V) ions are 126.88, 88.46, 356.21, 146.92, 51.28, and 166.10 mg/g, respectively. Based on a comparison of these adsorption capacities with reported values, **Mn-MOF-500** has excellent adsorption performance for these six ions (Table 3) (Liu and Zhang, 2015; Veenhuyzen, et al., 2021; Zhou, et al., 2021; Biswas, et al., 2007; Xu, et al., 2009; Köse and Kivanç, 2011; Anirudhan, et al., 2006; Liu, et al., 2021; Xie, et al., 2021; Zhang, et al., 2021d; Ahmed, et al., 2020; Xu, et al., 2021; Wang, et al., 2019a; Shi, et al., 2021; Wu, et al., 2019a; Wang, et al., 2021c; Liu, et al., 2020b; He, et al., 2020; Zhang, et al., 2021a; Zhang, et al., 2021b; Jin, et al., 2021; Wang, et al., 2021a; Pervez, et al., 2021; Lin, et al., 2019; Mudzielwana, et al., 2019; Dong, et al., 2020; Mahato, et al., 2021; Wang, et al., 2019b; Salih, et al., 2019).

3.3.3. Adsorption kinetics

The data were fitted to the pseudo-first-order (PFO) and pseudo-second-order (PSO) kinetic models at 288, 298, and 308 K, and the results are shown in Table 4 and Fig. 4.

For the adsorption of PO_4^{3-}, the PSO model fitted the data best: R^2 values are 0.94, 0.93, and 0.91 at 288, 298, and 308 K, respectively. Thus, the adsorption rate is proportional to the square of the concentration, and the adsorption process is based on chemisorption.

For Cd(II), Pb(II), and Cu(II) ions, adsorption by **Mn-MOF-500** can be divided into three stages: fast, slow, and equilibrium adsorption stages. With increase in temperature, the adsorption rates for Cd(II), Pb(II), and Cu(II) ions also accelerated, and the time to reach saturation was reduced. For Cd(II) adsorption, the PSO model fitted the data best, suggesting chemisorption. For Pb(II) and Cu(II) ions, the PFO model fitted best. The R^2 for the PSO was greater than 0.9, indicating that the adsorption of Pb(II) and Cu(II) ions by **Mn-MOF-500** is mainly physisorption supplemented by chemisorption.

Table 3 $q_{\max}$ of PO_4^{3-}, Cd(II), Pb(II), Cu(II), As(III), and As(V) by different adsorbents.

ions	adsorbent	q_m(mg/g)	Ref
PO_4^{3-}	**Mn-MOF-500**	126.88	This work
	La(III)-loaded saponified orange waste	14.00	Biswas, et al., 2007
	Zr-treated chitosan beads	60.60	Liu and Zhang 2015
	Modified wheat straw	22.90	Xu, et al., 2009
	Calcined waste eggshell	32.60	Köse and Kivanç 2011
	Banana stem (modified with DMAHPb)	23.60	Anirudhan, et al., 2006
Cd(II)	**Mn-MOF-500**	88.46	This work
	RHBC	81.3	Liu, et al., 2021
	AAM-MSM	78.1861	Xie, et al., 2021
	MAC-300	73.3	Zhang, et al., 2021d
	OCT-VER	69.595	Ahmed, et al., 2020
	HA-Fe-PILC	32.15	Xu, et al., 2021
Pb(II)	**Mn-MOF-500**	356.21	This work
	GO	273.0	Wang, et al., 2019a
	waste activated sewage sludge	307	Veenhuyzen, et al., 2021
	MnO_2/PDA/Fe_3O_4	205.07	Shi, et al., 2021
	P-MCS	151.06	Wu, et al., 2019a
	BC400	124.7	Wang, et al., 2021c
Cu(II)	**Mn-MOF-500**	146.92	This work
	A-Si/Mn-CRBC	141.76	Liu, et al., 2020b
	PVA-CS-EDTA	127.81	He, et al., 2020
	TSC-PVA	82.36	Zhang, et al., 2021a
	CMBC600	70.42	Zhang, et al., 2021b
	LESS600	65.61	Jin, et al., 2021
As(III)	**Mn-MOF-500**	51.28	This work
	FRKF	37.4	Wang, et al., 2021a
	α-FeOOH@GCA	32.19	Pervez, et al., 2021
	FMLBC3	15.34	Lin, et al., 2019
	SMK	2.33	Mudzielwana, et al., 2019
	PSMPs	1.12	Dong, et al., 2020
As(V)	**Mn-MOF-500**	166.10	This work
	S-nZVI@ZSM-5	161.66	Zhou, et al., 2021
	ZnO/AlSBA-15	123.99	Mahato, et al., 2021
	MCS/ZnO@Alg	63.69	Wang, et al., 2019b
	α-FeOOH@GCA	61.91	Pervez, et al., 2021
	CSD beads	44.07	Salih, et al., 2019

Table 4 Fitting relevant parameters of the **Mn-MOF-500** adsorption PO_4^{3-}, Cd(II), Pb(II), Cu(II), As(III), and As(V) kinetic model.

Ions	T (K)	q_{maxEX}* (mg/g)	pseudo-first-order			pseudo-second-order		
			k (/min)	q_e (mg/g)	R^2	k [g/(mg min)]	q_e (mg/g)	R^2
PO_4^{3-}	288	30.38	5.14	28.30	0.69	032	30.51	0.94
	298	31.99	5.99	29.79	0.68	0.33	32.19	0.93
	308	33.67	6.92	31.42	0.65	0.34	34.12	0.91
Cd(II)	288	7.26	5.39	6.98	0.87	1.33	7.37	0.97
	298	7.32	7.41	7.13	0.92	1.91	7.45	0.99
	308	7.41	9.36	7.21	0.84	2.62	7.49	0.97
Pb(II)	288	37.34	2.49	37.31	0.99	0.08	39.49	0.98
	298	37.42	4.15	37.54	0.98	0.15	38.82	0.96
	308	37.45	8.62	37.38	0.98	0.37	38.20	0.92
Cu(II)	288	37.09	2.48	36.92	0.99	0.08	39.26	0.94
	298	37.26	3.46	37.29	0.99	0.12	38.96	0.92
	308	37.40	4.63	37.35	0.99	0.17	38.77	0.92
As(III)	288	7.18	3.28	6.94	0.92	0.72	7.37	0.96
	298	7.29	3.61	7.01	0.89	0.82	7.44	0.96
	308	7.37	5.99	7.18	0.93	1.44	7.52	0.98
As(V)	288	12.47	1.69	12.46	0.99	0.15	13.28	0.98
	298	13.76	1.80	13.82	0.99	0.14	14.67	0.97
	308	14.27	2.06	14.40	0.99	0.17	15.14	0.96

Note:* q_{maxEX} means experimental value q_{max}.

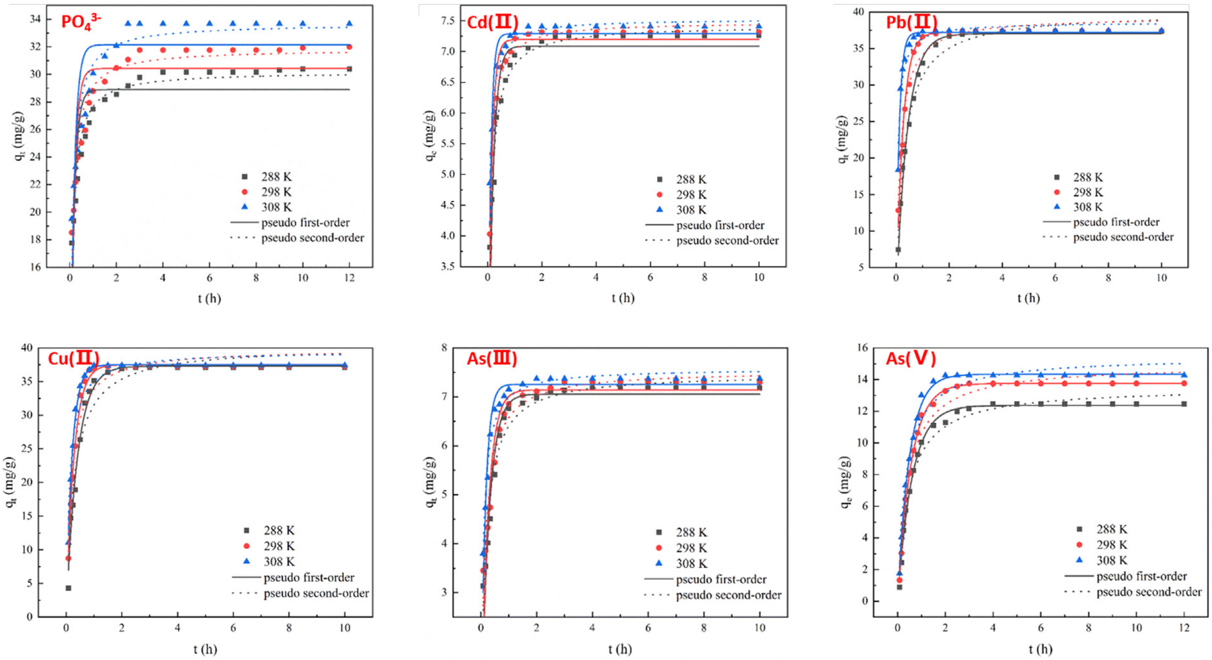

Fig. 4 Pseudo-first-order kinetic and Pseudo-second-order kinetic nonlinear dynamics fitting of **Mn-MOF-500** at 288.15 K, 298.15 K, and 308.15 K.

For As(III), the fitting to the PSO model was better than that to the PFO model, and the equilibrium adsorption (q_e) value calculated by the PSO kinetic model is close to the experimental q_{maxEX}, indicating that the adsorption of As(III) is chemisorption.

For As(V), the PFO model fitted best, yielding R_2 values are 0.99, 0.99, and 0.99 at 288, 298, and 308 K, respectively, whereas those for the PSO model were 0.98, 0.97, and 0.96 at 288, 298, and 308 K, respectively. The fitting coefficients for the two kinetic models are both higher 0.95, suggesting a mix of physi- and chemisorptions.

3.3.4. Desorption and regeneration experiments

As shown in Fig. S4, the sorbent showed good recyclability for the sorption of Cd(II), Pb (II), and Cu(II) ions. After four cycles, the sorption capacities of Cd(II), Pb(II), and Cu(II) ions were 78.97%, 82.7%, and 79.02%, respectively. For PO_4^{3-}, As(III), and As(V) ions, the sorption performance was not good on cycling, suggesting their poor desorption. Therefore, future experiments, investigation of desorption agents is required.

3.4. Effect of carbonisation

Water solubility analysis (see Supporting Material, Section 1.2.5 for experimental steps) showed that **Mn-MOF** was soluble in water, suggesting that it contains many hydrophilic groups and is unsuitable for wastewater treatment. In contrast, **Mn-MOF-500** showed good water stability, indicating that carbonisation converts the **Mn-MOF** to a water-stable material.

The PXRD patterns of **Mn-MOF** and **Mn-MOF-500** are shown in Fig. 5. The experimental pattern is consistent with the database pattern, indicating high purity and crystallinity. In contrast, the PXRD patterns of **Mn-MOF-500** contain peak shifts, indicating a reduction in crystallinity on carbonisation.

The Brunauer–Emmett–Teller (BET) nitrogen adsorption–desorption isotherm results are shown in Fig. S5. The BET specific surface area of **Mn-MOF** is 0.82 m^2/g, the average pore size is 34.82 nm, and the average mesopore diameter is 5.36 nm. After carbonisation, these values were 11.83 m^2/g, 25.15 nm, and 34.08 nm, respectively. Compared with that of **Mn-MOF**, the BET specific surface area of **Mn-MOF-500** is 14 times larger than that of **Mn-MOF**. Although the average pore size is decreased, the average mesoporous diameter of **Mn-MOF-500** is six times larger than that of **Mn-MOF**, indicating that high-temperature carbonisation modification can increase the specific surface area and mesopore size, which is conducive to enhancing the adsorption performance of **Mn-MOF-500**.

The thermogravimetric analysis (TGA) results are shown in Fig. S6. At 200 °C, the weight loss rate of **Mn-MOF** increased. At 650 °C, the weight of **Mn-MOF** was only 30% of the original weight. Thus, decomposition starts at 200 °C, probably as a result of the loss of DMF molecules. The boiling point of DMF is 153 °C, but the loss at 200 °C is likely a result of the interaction between Mn(II) ions and DMF molecules. At 258 °C, the weight loss of the **Mn-MOF** was 36.2% (theoretical weight loss of 36.8% based on the loss of two coordination DMF molecules). In contrast, **Mn-MOF-500** showed greater thermal stability, indicating that no coordinated DMF molecules are present. Therefore, the TGA results indicate that carbonisation damaged the structure of **Mn-MOF**.

SEM imaging was carried out using a JMS-7900 scanning electron microscope, as shown in Fig. 6a and b. Comparative analysis of the morphology of **Mn-MOF** and **Mn-MOF-500** shows that the former is composed of regular tetrahedral particles before carbonisation. In contrast, **Mn-MOF-500** is fluffy and porous. In addition, the colour changed (Fig. 6c and d), and the single crystalline structure was lost, further indicating that carbonisation destroys the structure of **Mn-MOF**.

The XPS results are shown in Fig. 7 and show that the elemental contents were not changed by carbonation.

3.5 Effects of ion adsorption

Mn-MOF-500, **Mn-MOF-500-P**, **Mn-MOF-500-Cd(II)**, **Mn-MOF-500-Pb(II)**, **Mn-MOF-500- Cu(II)**, **Mn-MOF-500-As(III)**, **and Mn-MOF-500-As(V)** were characterised by PXRD, and the results are shown in Fig. S7. After adsorption, the main peaks corresponding to the **Mn-MOF-500** remain, indicating that adsorption does not alter the structure. Jade 6 was used to analyse the PXRD data.

Based on the peaks at 14.676°, 11.711°, 11.218°, 11.393°, 11.445°, and 11.081°, PO_4^{3-}, $Cd(OH)_2$, PbO and $Pb(OH)_2$, $Cu(OH)_2$, $Mn_3(AsO_4)_2$, and $MnHAsO_4$ were present. In addition, the FTIR spectra of pristine **Mn-MOF-500** and those after adsorption are shown in Fig. S8. There are no obvious changes before and after adsorption, suggesting that **Mn-MOF-500** is stable and recyclable. Next, XPS was used to analyse the samples after adsorption, as shown in Fig. 8. For P, Cd(II), Pb(II), Cu(II), As(III), and As(V), the P2p peak at 133.92 eV indicates PO_4^{3-}; Cd $3d_{5/2}$ and Cd $3d_{3/2}$ peaks at 405.63 and 412.36 eV, respectively, indicate $Cd(OH)_2$; Pb $4f_{7/2}$ and Pb $4f_{5/2}$ peaks at 139.08 and 143.94 eV, indicate PbO and $Pb(OH)_2$, respectively; Cu $2p_{3/2}$ peak at 934.79 eV indicate $Cu(OH)_2$; As 3d peak at

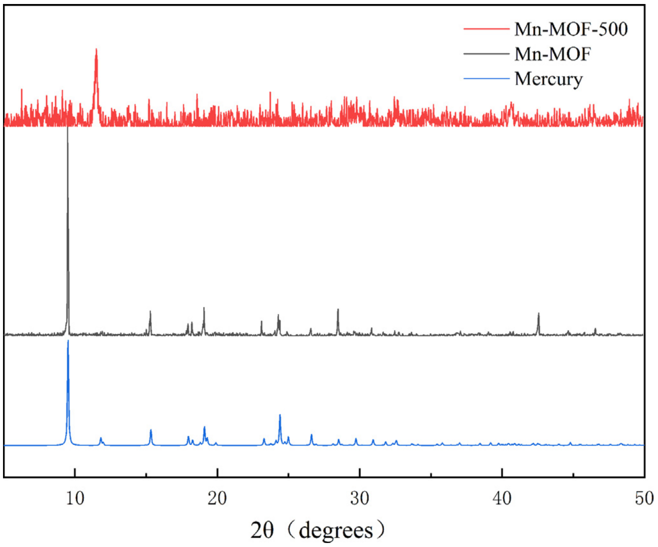

Fig. 5 XRD image of Mn-MOF and Mn-MOF-500.

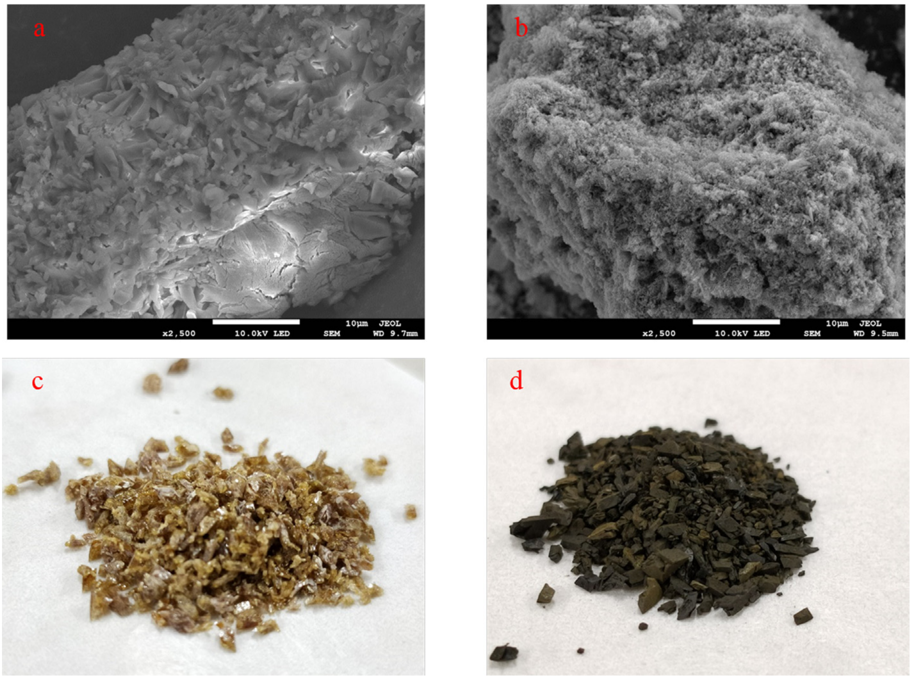

Fig. 6 SEM image of **Mn-MOF**(a) and **Mn-MOF-500**(b), Solid sample drawing of **Mn-MOF**(c) and **Mn-MOF-500**(d).

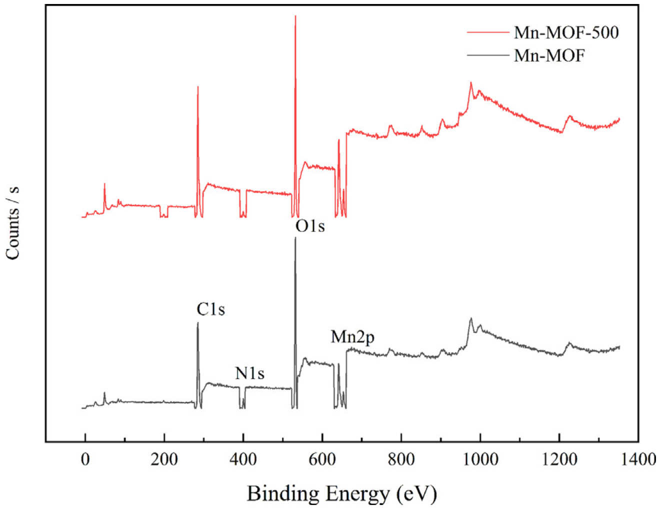

Fig. 7 Full XPS spectra of Mn-MOF and Mn-MOF-500.

48.80 eV indicates Mn$_3$(AsO$_3$)$_2$, and As 3d peaks at 45.10 and 48.75 eV, respectively, indicate MnHAsO$_4$. The SEM images of the materials after adsorption are shown in Fig. S9, revealing few changes to the structure after adsorption, suggesting the suitability of this material for industrial wastewater treatment.

3.6. Analysis of Mn-MOF-500 adsorption mechanism

The adsorption mechanism is shown in Fig. 9. Adsorption performance and mechanism of **Mn-MOF-500** on PO$_4^{3-}$: the research shown that the maximum adsorption capacity of **Mn-MOF-500** on PO$_4^{3-}$ was 126.66 mg/g, and its adsorption process conforms to Langmuir model and quasi second-order kinetic model. This adsorption process was single-molecule layer chemical adsorption. Dynamic adsorption experimental analysis shown that **Mn-MOF-500** had strong adsorption persistence on PO$_4^{3-}$, which was conducive to later industrial promotion and research. It was found that P was adsorbed on **Mn-MOF-500** in the form of PO$_4^{3-}$ by XRD, IR, XPS and SEM.

Adsorption performance and mechanism of **Mn-MOF-500** on Cd(Ⅱ), Pb(Ⅱ) and Cu(Ⅱ): the study shown that the maximum adsorption capacity of **Mn-MOF-500** on Cd(Ⅱ), Pb(Ⅱ) and Cu(Ⅱ) were 88.46, 356.21 and 146.92 mg/g, respectively. The isothermal adsorption experiments of Cd (II), Pb (II) and Cu (II) by **Mn-MOF-500** and the fitting degree of Langmuir model were higher than that of Freundlich model. In

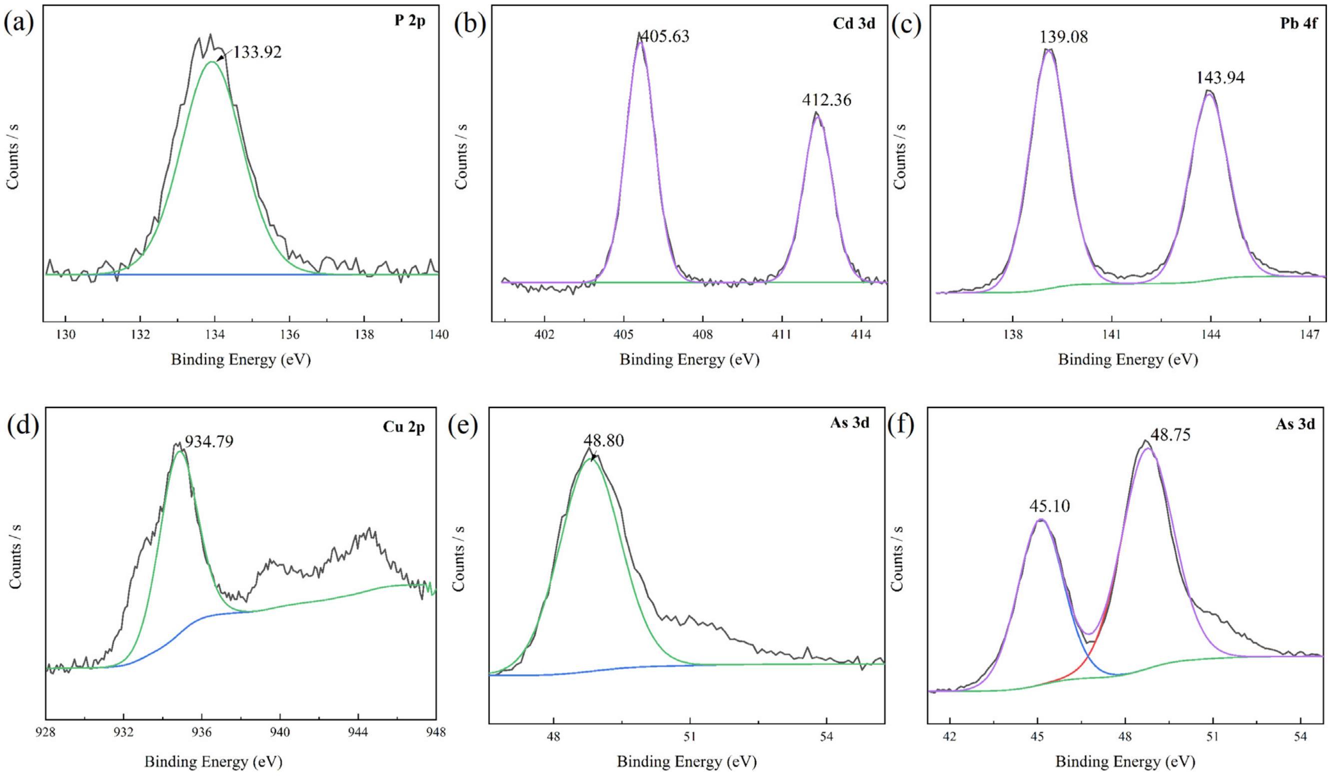

Fig. 8 Fine spectrum of PO_4^{3-}, Cd(II), Pb(II), Cu(II), As(III), and As(V) after adsorption by Mn-MOF-500.

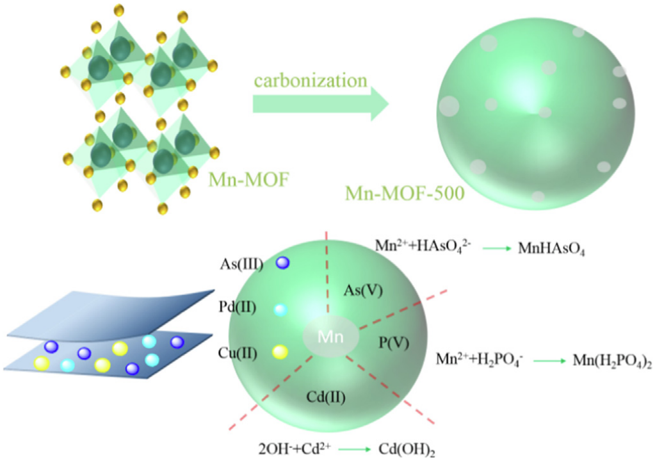

Fig. 9 Mn-MOF-500 adsorption mechanism.

the kinetic experiments, the adsorption process of Cd (II) by **Mn-MOF-500** only conformed to the quasi second-order kinetic model, and the adsorption process of Pb (II) and Cu (II) by **Mn-MOF-500** conformed to both the quasi first-order kinetic model and the quasi second-order kinetic model, indicating that the adsorption mechanism of Cd(II) by **Mn-MOF-500** was monolayer chemisorption, The adsorption of Pb (Ⅱ) and Cu (Ⅱ) by **Mn-MOF-500** were the result of the interaction of monolayer chemisorption and pore physical adsorption. According to the experimental data of adsorption and desorption, **Mn-MOF-500** shown good cyclic regeneration for Cd (Ⅱ), Pb (Ⅱ) and Cu (Ⅱ). It was found that Cd (Ⅱ), Pb (Ⅱ) and Cu (Ⅱ) were adsorbed on **Mn-MOF-500** in the form of Cd $(OH)_2$, PbO, $Pb(OH)_2$ and $Cu(OH)_2$ respectively by XRD, IR, XPS and SEM.

Adsorption performance and mechanism of **Mn-MOF-500** for As(III), and As(V): the study shown that the maximum adsorption capacity of **Mn-MOF-500** for As(III), and As(V) was 51.28 and 166.10 mg/g respectively. The adsorption process of **Mn-MOF-500** on As(III), and As(V) was higher that of Langmuir model than Freundlich model. The adsorption process of **Mn-MOF-500** on As (Ⅲ) only conforms to the quasi second-order kinetic model. The adsorption process of **Mn-MOF-500** on As(V) conformed to both the quasi first-order kinetic model and the quasi second-order kinetic model, indicating that the adsorption of **Mn-MOF-500** on As(III) was a single molecular layer chemisorption. The adsorption of As (V) on **Mn-MOF-500** has both monolayer chemisorption and pore physical adsorption. It was found that As(III), and As (V) were adsorbed on **Mn-MOF-500** in the form of $Mn_3(AsO_3)_2$ and $MnHAsO_4$ by XRD, IR, XPS and SEM.

4. Conclusion

A water-soluble metal–organic framework material, **Mn-MOF**, was prepared using a solvothermal method. To reduce water solubility, direct carbonisation was used. The optimal carbonisation temperature was found to be 500 °C. Subsequently, **Mn-MOF** and **Mn-MOF-500** were characterised using XRD, BET, XPS, and other methods, revealing that carbonisation destroyed the internal structure of **Mn-MOF** but did not affect the constituent elements. After carbonisation, **Mn-MOF-500** had increased stability in water, the BET specific surface was increased 14 times to 11.83 m^2/ g, and the size of the mesopores was expanded by six times to 34.08 nm, both of which are conducive to enhancing adsorption performance.

The maximum adsorption capacity of **Mn-MOF-500** for PO_4^{3-}, Cd (II), Pb(II), Cu(II), As(III), and As(V) was 126.66, 88.46, 356.21, 146.92, 51.28 and 166.10 mg/g, respectively. Compared with published research results, The maximum adsorption capacity of **Mn-MOF-500** for PO_4^{3-}, Cd(II), Pb(II), Cu(II), As(III), and As(V) are higher than the vast majority of reported adsorption materials. Further, XRD, IR, XPS, and SEM analysis revealed that PO_4^{3-}, Cd (II), Pb (II), Cu (II), As(III), and As(V) were adsorbed on **Mn-MOF-500** in the form of PO_4^{3-}, $Cd(OH)_2$, PbO, $Pb(OH)_2$, $Cu(OH)_2$, $Mn_3(AsO_3)_2$, and $MnHAsO_4$, respectively.

Adsorption for phosphorous, Cd(II), Pb(II), Cu(II), As(III), and As(V) were consistent with the Langmuir model. In addition, the fitting of the kinetic data for phosphorous, Cd(II), Pb(II), and Cu(II) conformed to pseudo-second-order kinetic model, pseudo second-order kinetic model, quasi first-order kinetic model and the pseudo first-order kinetic model, respectively. indicating that phosphorous, Cd(II), Pb(II) and Cu(II) were adsorbed by monolayer chemisorptions, monolayer chemisorptions, mainly physisorption and mainly physisorption, respectively. In addition, the adsorption of As(III) conforms to the pseudo-second-order kinetic model, whereas that of As(V) conforms to both the pseudo-first-order kinetic model and the pseudo-second-order kinetic model, indicating that As(III) was adsorbed by monolayer chemisorption, whereas As(V) is adsorbed by both monolayer chemisorption and physisorption in the pores. Recycling experiments with Cd(II), Pb(II), and Cu(II) revealed the good recycling performance of this material.

Authors contributions

Investigation: Zhao Chen has completed the synthesis of complexes **Mn-MOF** and **Mn-MOF-n** (300, 400, 500, 600, 700, 800 °C), elemental analysis, IR and single-crystal structures analysis of complex **Mn-MOF**, and Adsorption experiment and characterization, Analysis of **Mn-MOF-500** adsorption mechanism. Yating Chen has completed the refine the structure of **Mn-MOF**, Selection of optimum modification temperature, Adsorption performance analysis of **Mn-MOF-500**, Comparative analysis of carbonization before and after, Characterization of **Mn-MOF-500** before and after adsorption.

CRediT authorship contribution statement

Yating Chen: . **Zhao Chen:** . **Lingyu Yuan:** . **Yu Xiao:** Resources, Funding acquisition. **Shu-Hua Zhang:** Writing – review & editing, Supervision, Resources, Project administration, Funding acquisition. **Ning Li:** Writing – original draft, Supervision, Project administration.

Declaration of Competing Interest

The authors declare that they have no known competing financial interests or personal relationships that could have appeared to influence the work reported in this paper.

Acknowledgments

This work was supported by the Nature Science Foundation of China (No. 21861014), and Projects of Talents Recruitment of Guangdong University of Petrochemical Technology (2020rc033, 2020rc035).

Appendix A. Supplementary data

Supplementary data to this article can be found online at https://doi.org/10.1016/j.arabjc.2023.104950.

References

Ahmed, Z., Wu, P., Jiang, L., Liu, J., Ye, Q., Yang, Q., Zhu, N., 2020. Enhanced simultaneous adsorption of Cd (II) and Pb (II) on octylamine functionalized vermiculite. Colloid. Surf. A. 604, 125285.

An, H.J., Bhadra, B.N., Khan, N.A., Jhung, S.H., 2018. Adsorptive removal of wide range of pharmaceutical and personal care products from water by using metal azolate framework-6-derived porous carbon. Chem. Eng. J. 343, 447–454.

Anirudhan, T.S., Noeline, B.F., Manohar, D.M., 2006. Phosphate removal from wastewaters using a weak anion exchanger prepared from a lignocellulosic residue. Environ. Sci. Technol. 40, 2740–2745.

Bhadra, B.N., Ahmed, I., Kim, S., Jhung, S.H., 2017. Adsorptive removal of ibuprofen and diclofenac from water using metal-organic framework-derived porous carbon. Chem. Eng. J. 314, 50–58.

Biswas, B.K., Inoue, K., Ghimire, K.N., Ohta, S., Harada, H., Ohto, K., Kawakita, H., 2007. The adsorption of phosphate from an aquatic environment using metal-loaded orange waste. J. Colloid Interf. Sci. 312, 214–223.

Chao, S., Xia, Q., Wang, Y., Li, W., Chen, W., 2020. Pristine S, N-containing Mn-based metal organic framework nanorods enable efficient oxygen reduction electrocatalysis. Dalton Trans. 49, 4336–4342.

Chen, Z., Li, P., Zhang, X., Li, P., Wasson, M.C., Islamoglu, T., Farha, O.K., 2019. Reticular access to highly porous acs-MOFs with rigid trigonal prismatic linkers for water sorption. J. am. Chem. Soc. 141, 2900–2905.

Dolomanov, O.V., Bourhis, L.J., Gildea, R.J., Howard, J.A.K., Puschmann, H., 2009. OLEX2: a complete structure solution, refinement and analysis program. J. Appl. Crystallogr. 42 (2), 339–341.

Dong, Y., Gao, M., Song, Z., Qiu, W., 2020. As (III) adsorption onto different-sized polystyrene microplastic particles and its mechanism. Chemosphere 239, 124792.

Dutta, A., Pan, Y., Liu, J.Q., Kumar, A., 2021. Multicomponent isoreticular metal-organic frameworks: principles, current status and challenges. Coordin. Chem. Rev. 445, 214074.

Fosso-Kankeu, E., Mulaba-Bafubiandi, A.F., Mamba, B.B., Barnard, T.G., 2011. Prediction of metal-adsorption behaviour in the remediation of water contamination using indigenous microorganisms. J. Environ. Manage. 92, 2786–2793.

He, W., Yu, Q., Wang, N., Ouyang, X.K., 2020. Efficient adsorption of Cu (II) from aqueous solutions by acid-resistant and recyclable ethylenediamine tetraacetic acid-grafted polyvinyl alcohol/chitosan beads. J Mol. Liq. 316, 113856.

Jin, Y., Zhang, M., Jin, Z., Wang, G., Li, R., Zhang, X., Liu, X., Qu, J., Wang, H., 2021. Characterization of biochars derived from various spent mushroom substrates and evaluation of their adsorption performance of Cu (II) ions from aqueous solution. Environ. Res. 196, 110323.

Köse, T.E., Kivanç, B., 2011. Adsorption of phosphate from aqueous solutions using calcined waste eggshell. Chem. Eng. J. 178, 34–39.

Krupskaya, L.T., Zvereva, V.P., 2014. Bioaccumulation of heavy metals with environmental objects and assessment of health risks (the former mining enterprise Khingansky GOK as an example). Russ. J. Gen. Chem + . 84, 2542–2544.

Li, H., Eddaoudi, M., O'Keeffe, M., Yaghi, O.M., 1999. Design and synthesis of an exceptionally stable and highly porous metal-organic framework. Nature 402, 276–279.

Li, J.J., Wang, C.C., Guo, J., Cui, J.R., Wang, P., Zhao, C., 2018. Three coordination compounds based on tris (1-imidazolyl) benzene: Hydrothermal synthesis, crystal structure and adsorption performances toward organic dyes. Polyhedron 139, 89–97.

Lin, L., Zhang, G., Liu, X., Khan, Z.H., Qiu, W., Song, Z., 2019. Synthesis and adsorption of Fe-Mn-La- impregnated biochar composite as an adsorbent for As(III) removal from aqueous solutions. Environ. Pollut. 247, 128–135.

Liu, J.Q., Luo, Z.D., Pan, Y., Singh, A.K., Trivedi, M., Kumar, A., 2020a. Recent developments in luminescent coordination polymers: Designing strategies, sensing application and theoretical evidences. Coordin. Chem. Rev. 406, 213145.

Liu, P., Rao, D., Zou, L., Teng, Y., Yu, H., 2021. Capacity and potential mechanisms of Cd (II) adsorption from aqueous solution by blue algae-derived biochars. Sci. Total. Environ. 767, 145447.

Liu, J., Yang, X., Liu, H., Cheng, W., Bao, Y., 2020b. Modification of calcium-rich biochar by loading Si/Mn binary oxide after NaOH activation and its adsorption mechanisms for removal of Cu (II) from aqueous solution. Colloid. Surface. A. 601, 124960.

Liu, X., Zhang, L., 2015. Removal of phosphate anions using the modified chitosan beads: adsorption kinetic, isotherm and mechanism studies. Powder. Technol. 277, 112–119.

Mahato, B.N., Krithiga, T., Thangam, M.M., 2021. Rapid adsorption of As (V) from aqueous solution by ZnO embedded in mesoporous aluminosilicate nanocomposite adsorbent: parameter optimization, kinetic, and isotherms studies. Surf. Interfaces. 23, 100636.

Mbonu I.J., Abiola O.K., 2021. Adsorption of Nitrogen on Mn(II) Metal-Organic Framework Nanoparticles JOTCSA. 8(3) 941-952.

Mudzielwana, R., Gitari, M.W., Ndungu, P., 2019. Performance evaluation of surfactant modified kaolin clay in As (III) and As (V) adsorption from groundwater: adsorption kinetics, isotherms and thermodynamics. Heliyon 5, e02756.

Oveisi, M., Asli, M.A., Mahmoodi, N.M., 2018. MIL-Ti metal-organic frameworks (MOFs) nanomaterials as superior adsorbents: Synthesis and ultrasound-aided dye adsorption from multicomponent wastewater systems. J. Hazard. Mater. 347, 123–140.

Pervez, M.N., Fu, D., Wang, X., Bao, Q., Yu, T., Naddeo, V., Tan, H., Cao, C., Zhao, Y., 2021. A bifunctional α-FeOOH@ GCA nanocomposite for enhanced adsorption of arsenic and photo Fenton-like catalytic conversion of As (III). Environ. Technol. Inno. 22, 101437.

Rios, C.A., Williams, C.D., Roberts, C.L., 2008. Removal of heavy metals from acid mine drainage (AMD) using coal fly ash, natural clinker and synthetic zeolites. J Hazard. Mater. 156, 23–35.

Salih, S.S., Mahdi, A., Kadhom, M., Ghosh, T.K., 2019. Competitive adsorption of As (III) and As (V) onto chitosan/diatomaceous earth adsorbent. J. Environ. Chem. Eng. 7, 103407.

Sheldrick, G.M., 2015. SHELXT–Integrated space-group and crystal-structure determination. Acta. Crystallogr. A. 71, 3–8.

Shi, S., Xu, C., Dong, Q., Wang, Y., Zhu, S., Zhang, X., Chow, W.T., Wang, X., Zhu, L., Zhang, L., Xu, D., 2021. High saturation magnetization MnO_2/PDA/Fe_3O_4 fibers for efficient Pb (II) adsorption and rapid magnetic separation. Appl. Surf. Sci. 541, 148379.

Song, J.Y., Jhung, S.H., 2017. Adsorption of pharmaceuticals and personal care products over metal-organic frameworks functionalized with hydroxyl groups: quantitative analyses of H-bonding in adsorption. Chem. Eng. J. 322, 366–374.

Türker, O.C., Türe, C., Böcük, H., Yakar, A., 2014. Constructed wetlands as green tools for management of boron mine wastewater. Int. J. Phytoremediat. 16, 537–553.

Veenhuyzen, B.V., Tichapondwa, S., Hörstmann, C., Chirwa, E., Brink, H.G., 2021. High capacity Pb (II) adsorption characteristics onto raw-and chemically activated waste activated sludge. J. Hazard. Mater. 416, 125943.

Vignesh, K., Priyanka, R., Hariharan, R., Rajarajan, M., Suganthi, A., 2014. Fabrication of CdS and $CuWO_4$ modified TiO_2 nanoparticles and its photocatalytic activity under visible light irradiation. J. Ind. Eng. Chem. 20, 435–443.

Vymazal, J., 2007. Removal of nutrients in various types of constructed wetlands. Sci. Total. Environ. 380, 48–65.

Wang, J., Li, Y., Lv, Z., Xie, Y., Shu, J., Alsaedi, A., Hayat, T., Chen, C., 2019a. Exploration of the adsorption performance and mechanism of zeolitic imidazolate framework-8@ graphene oxide for Pb (II) and 1-naphthylamine from aqueous solution. J. Colloid. Interf. Sci. 542, 410–420.

Wang, S., Lu, Y., Ouyang, X.K., Liang, X.X., Yu, D., Yang, L.Y., Huang, F., 2019b. Fabrication of chitosan-based MCS/ZnO@ Alg gel microspheres for efficient adsorption of As (V). Int. J. Biol. Macromol. 139, 886–895.

Wang, Z., Xu, J., Yellezuome, D., Liu, R., 2021c. Effects of cotton straw-derived biochar under different pyrolysis conditions on Pb (II) adsorption properties in aqueous solutions. J. Anal. Appl. Pyrol. 157, 105214.

Wang, D., Yi, C., Xu, M., Park, J.S., Kim, D., Shin, C.H., Ryu, M.H., Zhao, Y., 2021a. Adsorption of As (III) and As (V) by using the Fenton reaction modified kapok fiber. J. Environ. Chem. Eng. 9, 105918.

Wang, S.T., Zheng, X., Zhang, S.H., Li, G.Z., Xiao, Y., 2021b. A study of GUPT-2, a water-stable zinc-based metal–organic framework as a highly selective and sensitive fluorescent sensor in the detection of Al^{3+} and Fe^{3+} ions. CrstEngComm 23, 4059–4068.

Wu, Y.P., Tian, J.W., Liu, S., Li, B., Zhao, J., Ma, L.F., Bu, X., 2019b. Bi-Microporous Metal-Organic Frameworks with Cubane $[_M4(OH)_4]$ (M = Ni, Co) Clusters and Pore-Space Partition for Electrocatalytic Methanol Oxidation Reaction. Angew. Chem. 131, 12313–12317.

Wu, D., Wang, Y., Li, Y., Wei, Q., Hu, L., Yan, T., Feng, R., Yan, L., Du, B., 2019a. Phosphorylated chitosan/$CoFe_2O_4$ composite for the efficient removal of Pb (II) and Cd (II) from aqueous solution: adsorption performance and mechanism studies. J. Mol. Liq. 277, 181–188.

Xie, X., Zhao, X., Luo, X., Su, T., Zhang, Y., Qin, Z., Ji, H., 2021. Mechanically activated starch magnetic microspheres for Cd (II) adsorption from aqueous solution. Chinese. J. Chem. Eng. 33, 40–49.

Xu, X., Gao, B., Wang, W., Yue, Q., Wang, Y., Ni, S., 2009. Adsorption of phosphate from aqueous solutions onto modified wheat residue: characteristics, kinetic and column studies. Colloid. Surface. B. 70, 46–52.

Xu, H., Hu, X., Chen, Y., Li, Y., Zhang, R., Tang, C., Hu, X., 2021. Cd (II) and Pb (II) absorbed on humic acid-iron-pillared bentonite: kinetics, thermodynamics and mechanism of adsorption. Colloid. Surface. A. 612, 126005.

Xu, L., Kwon, Y.-U., Castro, B., Cunha-Silva, L., 2013. Novel Mn (II)-Based Metal−Organic Frameworks Isolated in Ionic Liquids. Cryst. Growth Des. 13, 1260–1266.

Yılmaz, A.E., Boncukcuoglu, R., Yılmaz, M.T., Kocakerim, M.M., 2005. Adsorption of boron from boron- containing wastewaters by ion exchange in a continuous reactor. J. Hazard. Mater. 117, 221–226.

Yu, C.X., Wang, K.Z., Li, X.J., Liu, D., Ma, L.F., Liu, L.L., 2020. Highly efficient and facile removal of Pb^{2+} from water by using a negatively charged azoxy-functionalized metal–organic framework. Cryst. Growth. Des. 20, 5251–5260.

Zhang, Z., Chen, Z., Xiao, Y., Yi, M., Zheng, X., Xie, M., Shen, M., 2021c. Study of the dynamic adsorption and the effect of the presence of different cations and anions on the adsorption of As (V) on GUT-3. Appl. Organomet. Chem. 35, e6289.

Zhang, S., Chen, Z., Zhou, T., Li, G., 2022. Zn Metal-Organic Framework with High Stability and Sorption Selectivity for CO_2. Organometallics 41, 829–835.

Zhang, Y., Kang, X., Guo, P., Tan, H., Zhang, S., 2022a. Studies on the removal of phosphate in water through adsorption using a novel Zn-MOF and its derived materials. Arab. J. Chem. 15 (8), 103955.

Zhang, C., Qin, Y., Ke, Z., Yin, L., Xiao, Y., Zhang, S., 2023. Highly efficient and facile removal of As(V) from water by using Pb-MOF with higher stable and fluorescence. Appl Organomet Chem. 37, e7066.

Zhang, Z., Wang, T., Zhang, H., Liu, Y., Xing, B., 2021d. Adsorption of Pb (II) and Cd (II) by magnetic activated carbon and its mechanism. Sci. Total. Environ. 757, 143910.

Zhang, L., Yang, F., Zhao, Y., Zhong, L., Gao, R., Zhang, X., Wang, T., Xue, J., 2021a. Preparation of thiosemicarbazide-modified polyvinyl alcohol and its selective adsorption of Cu (II). Colloid. Interfac. Sci. 43, 100377.

Zhang, P., Zhang, X., Yuan, X., Xie, R., Han, L., 2021b. Characteristics, adsorption behaviors, Cu (II) adsorption mechanisms by cow manure biochar derived at various pyrolysis temperatures. Bioresource. Technol. 331, 125013.

Zhou, C., Han, C., Min, X., Yang, T., 2021. Simultaneous adsorption of As (V) and Cr (VI) by zeolite supporting sulfide nanoscale zero-valent iron: Competitive reaction, affinity and removal mechanism. J. Mol. Liq. 338, 116619.